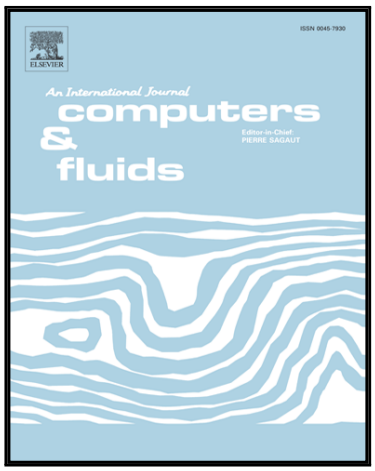

A Numerical Study of Liquid Atomization Regimes by means of Conservative Level-Set Simulations

Eugenio Schillaci, Oscar Antepara, Néstor Balcázar,
Joaquim Rigola Serrano, Assensi Oliva

PII: S0045-7930(18)30780-1
DOI: https://doi.org/10.1016/j.compfluid.2018.10.017
Reference: CAF 4034

To appear in: *Computers and Fluids*

Received date: 4 May 2018
Revised date: 7 August 2018
Accepted date: 14 October 2018

Please cite this article as: Eugenio Schillaci, Oscar Antepara, Néstor Balcázar, Joaquim Rigola Serrano, Assensi Oliva, A Numerical Study of Liquid Atomization Regimes by means of Conservative Level-Set Simulations, *Computers and Fluids* (2018), doi: https://doi.org/10.1016/j.compfluid.2018.10.017

Highlights

- Adoption of a CLS-AMR strategy to achieve the DNS of two-phase Liquid Jets.
- Validation in the context of 3D atomization by simulating Coaxial Liquid-Air Jets.
- DNS and study of Liquid Jets' features as function of several different parameters.
- Proposition of a complete break-up regimes map, entirely obtained from DNSs.
- Report of similarities and differences with respect to experimental studies.

A Numerical Study of Liquid Atomization Regimes by means of Conservative Level-Set Simulations

Eugenio Schillaci[a,*], Oscar Antepara[a,b], Néstor Balcázar[a,b], Joaquim Rigola Serrano[a], Assensi Oliva[a,*]

[a] *Heat and Mass Transfer Technological Center (CTTC), Universitat Politècnica de Catalunya - BarcelonaTech (UPC), ESEIAAT, Colom 11, E-08222 Terrassa, Barcelona, Spain*

[b] *Termo Fluids S.L., Av. Jacquard 97 1-E, 08222 Terrassa (Barcelona), Spain*

Abstract

In this work, a conservative level-set finite-volume solver for interface-capturing is employed to perform the direct numerical simulation of Liquid Jets discharging into a quiescent air chamber. The scope is to propose a complete break-up regimes map entirely obtained from numerical simulations. The solver accounts for an adaptive mesh refinement strategy to optimize the computational resources. The numerical model is firstly validated in the context of 3D atomization by simulating the behavior of 3D Coaxial Liquid-Air Jets. Next, we propose an overview of the physical behavior of Liquid Jets, mainly proceeding from theoretical and experimental works. Hence, we perform a series of simulations aimed at studying the variability of the Liquid Jet characteristics as function of selected input parameters. In particular, the

*Corresponding author. Tel.: +34 93 739 81 92; Fax: +34 93 739 89 20.
Email addresses: eugenio@cttc.upc.edu (Eugenio Schillaci), cttc@cttc.upc.edu (Assensi Oliva)

analyzed cases are characterized by variable values of Reynolds, Ohnesorge and Weber numbers. The patterns obtained in simulations are compared to the ones expected from bibliographic studies, situating each case on a break-up regime map. A general good agreement is found in the identification of the various break-up regimes and characteristic lengths, while the major differences have been highlighted and interpreted.

Keywords: two-phase liquid injection, instability and break-up phenomena, conservative level-set, adaptive mesh refinement

1. Introduction

The injection of a liquid flux into a quiescent air environment is a recurrent set-up in industrial applications. Some remarkable examples are the fuel injectors in Diesel engines, propulsion systems and some kinds of pharmaceutical sprays. However, the study of the liquid atomization processes is currently a problem not totally understood in the engineering field, due to the high complexity of the phenomena that lead to the generation and amplification of instabilities at the interface and to the complete pulverization of the liquid core —an introduction to the physical processes involved is available in Tryggvason et al. [1]. A correct numerical representation of such processes would bring great advances in the simulation of the related applications.

In the last decades, several numerical methods have been proposed to solve atomization problems, spacing between the three main classes of compu-

tational fluid dynamics (CFD) models. In Reynolds-averaged Navier-Stokes equations models (RANS) [2], the approach is based on a homogeneous formulation of the two-phase medium, and the transport of mean interface density is modeled by diffusion-like hypothesis, therefore neglecting the effect of the interaction between liquid structures [3]. LEIS (Large Eddy and Interface Simulations) methods combine the resolution of filtered Navier-Stokes equations (LES Models) with the tracking of the interface by means of the typical one-fluid formulations, as Level-Set or Volume-of-Fluid. For example, as in single-phase flows, Sagaut [4] applied a dynamic Smagorinsky model in under-resolved regions of the domain. Therefore, the flow variables in governing equations are considered to be the filtered variables by adding a sub-grid scale (SGS) stress term to the RHS of momentum equations. The main drawback of this method has been the difficulty of combining filtered equations with the representation of source terms, i.e. surface tension. However, there are recent developments related to the combination of LES with VoF for turbulent free-surface, bubbly flows and break-up phenomena, as discussed by Liovic and Lakehal [5]. The idea consists of grid-filtering each phase separately, and modeling the resulting SGS stresses as if they were isolated. However, special treatment may be necessary at the interface, taking advantage of the fact that the lighter phase perceives the interfaces like deformable walls. Here, Liovic and Lakehal showed that the effect of unresolved surface tension source terms is small compared to classic SGS stress term. Recently, Behzad et al. [6] demonstrated the reliability of LEIS models

by simulating the physical mechanism underlying the surface break-up of a liquid jet injected transversely on a cross flow at Re= 1200.

Finally, direct numerical simulation (DNS) approaches involve strict requirements in terms of computational resources, because of the numerous length scales involved in the phenomenon. That includes the correct representation of surface phenomena, such as the growth of waves and filaments, as well as the generation of drops of varying size in primary and secondary atomization processes. Therefore, as demonstrated by Shinjo and Umemura [7], the use of huge computational resources is needed to carry out the DNS of complete atomization phenomena. Nevertheless, these results allow to obtain detailed information and useful insights on the physics of atomizing two-phase flows. An early review on the DNS of two-phase atomizing flow was presented by Gorokhovski and Herrmann [3]. Instead, we present below some of the most recent contributions within this field. Between the others, Desjardins et al. [8] proposed a robust and mass conservative numerical method for the study of the turbulent atomization of a liquid Diesel jet, consisting in the injection of a high-velocity liquid into a still air chamber. In Desjardins et al. [9] the same method is used to perform further simulations of Diesel injectors. Moreover, they applied it to the simulation of coaxial jets —where the atomization of the liquid is assisted by the coaxial injection of a high-speed gas— obtaining a good agreement between experimental and numerical data in a wide range of situations. Ménard et al. [10] and Lebas et al. [11] contributed to the understanding of primary break-up in Diesel spray by

means of simulations, e.g. correctly representing the influence of gas temperature. Fuster et al. [12] studied the influence of the injector and the effect of vortices generation and swirling in high Reynolds number simulations of coaxial jets. Again, Shinjo and Umemura [7] performed simulations of liquid injection in still air, obtaining detailed insights on the formation of ligaments and drops during the primary atomization process. Delteil et al. [13] analyzed in detail the break-up of a water jet in the wind-induced regime. More recently, Salvador et al. [14] studied the influence of mesh size in Diesel spray simulations. Grosshans et al. [15] analyzed the influence of various parameters as nozzle turbulence, cavitation bubbles, density and viscosity liquid-gas ratio in the final size of droplets. Finally, Shao et al. [16] performed detailed simulations of the swirling liquid primary atomization process. However, all the works listed concentrate mainly on the detailed study of individual cases. To the best of the authors' knowledge, there is no reference that analyzes a wide range of cases —e.g. in terms of Reynolds or Weber number— by means of a generalizable numerical model, as happens on the contrary in experimental works (e.g. Badens et al. [17]).

In this work, the injection of a liquid flux in a quiescent air environment is studied by means of direct numerical simulations (DNS) for a large range of input parameters. The simulations are performed on the in-house platform *TermoFluids* [18]. The numerical framework employed solves the non-filtered Navier-Stokes equations on a collocated unstructured basis, while the interface-capturing is carried out by means of a conservative level-set (CLS)

technique [19]. The base fixed mesh is refined adaptively in order to obtain the required characteristic length in all the parts of the domain [20, 21, 22]. In Schillaci et al. [23] the inclusion of adaptive mesh refinement (AMR) into the existing CLS solver was verified and employed to obtain physical insights of a coaxial 2D turbulent jet. Further verifications and validations of the CLS method on fixed meshes and dynamic meshes have been reported in [19, 24, 25].

In the current work, the numerical framework is extended to the context of 3D atomization processes. Firstly, we propose a validation case, consisting in the simulation of two different coaxial liquid-gas 3D jets. In the analyzed cases the Reynolds number of the liquid jet varies between 600 and $\sim 1 \times 10^4$, while the Weber number, which indicates the aerodynamic pressure exerted by the gas on the liquid, ranges between 200 and 4.5×10^3. The numerical results are validated by using the empirical correlations obtained in experimental works by [26] and [27].

Secondly, the numerical platform is used to perform a detailed DNS study of the liquid injection into a quiescent gas chamber, main contribution of the current work. As an introduction, a general review on experimental and theoretical references on the atomization of liquid jets is proposed, in order to establish the basis for a complete comparison with the results already present in the literature. The case is analyzed for a wide range of physical parameters as the inlet velocity of the liquid and the surface tension coefficient. Our aim is to propose some additional insights to the atomization literature, by

carrying out an exhaustive array of cases, and taking into account the most influent input parameters. In all the cases, we analyzed the quantities that characterize the resulting physics, such as the intact length or the diameter of the drops. Hence, the various tests are placed on break-up regime maps as function of dimensionless parameters (Re_l, We_g and Oh), to be compared with the correlations found in the literature.

Hence, this Paper is organized as follows. In Sec. 2, the employed numerical method is explained. In Sec. 3, we present a numerical study of the coaxial jet set-up, in order to carry out a validation of the numerical framework in a 3D scenario characterized by instability and break-up phenomena. In Sec. 4, we review the literature dealing with the physics of the liquid injection. This serves as an introduction to Sec. 5, where we detail the simulations performed to identify the atomization regimes, analyzing similarities and differences between numerical results and reference data found in literature. Finally, we report all the obtained conclusions in Sec. 6.

2. Numerical Framework

The numerical method utilized in this work has been developed on the in-house platform *TermoFluids* [18] for CFD simulations. The method accounts for a finite-volume discretization of Navier-Stokes equations for momentum conservation on collocated unstructured meshes, and for a level-set description of the interface. Technical details on the discretization and implementation of the methods are detailed in Balcázar et al. [19].

In particular, the conservative level-set (CLS) method, as introduced by [19] in the framework of unstructured grids, is used for interface capturing. The interface is advected by means of the following equation

$$\frac{\partial \phi(\mathbf{x},t)}{\partial t} + \nabla \cdot (\phi(\mathbf{x},t)\mathbf{u}) = 0, \tag{1}$$

where $\phi(\mathbf{x},t)$ is the regularized distance function from the interface and $\mathbf{u}(\mathbf{x},t)$ is the velocity scalar field. At every time step, the level-set function is re-initialized in pseudo-time, τ, according to

$$\frac{\partial \phi}{\partial \tau} + \nabla \cdot \phi(1-\phi)\mathbf{n} = \nabla \cdot \varepsilon \nabla \phi \tag{2}$$

The proposed reinitialization equation accounts for a compressive flux term that keeps the interface sharp, and for a counter-diffusive term regulated by the empirical coefficient ε, that avoids the diffusion of $\phi(\mathbf{x},t)$. As numerical advantages of this model, the CLS method avoids the accumulation of mass conservation error, which is an issue inherent to standard level-set formulations, whereas an accurate computation of surface tension is achieved. Furthermore, the numerical formulation of the CLS methods [19, 28] is simpler in comparison to other interface-capturing approaches such as coupled level-set and volume-of-fluid method [29], which need to advect an indicator function together with a signed distance function, or in comparison to methods that need geometrical algorithms for interface reconstruction [30, 31].

The velocity scalar field, $\mathbf{u}(\mathbf{x},t)$, needed for the advection of the interface,

is derived from the resolution of Navier-Stokes equations in the incompressibility and variable properties limit (density, viscosity). In a domain occupied by two incompressible fluids separated by an interface, the fluids are governed by the following equations

$$\nabla \cdot \mathbf{u} = 0, \tag{3}$$

$$\frac{\partial(\rho \mathbf{u})}{\partial t} + \nabla \cdot (\rho \mathbf{u}\mathbf{u}) = -\nabla p + \nabla \cdot (\mu[\nabla \mathbf{u} + (\nabla \mathbf{u})^T]) + \mathbf{S}_\sigma, \tag{4}$$

where p is the pressure, ρ is the density, μ is the dynamic viscosity and $\mathbf{S}_\sigma$ is a volumetric source taking into account the effect of surface tension. The convective term, $\nabla \cdot (\rho \mathbf{u}\mathbf{u})$, is discretized by means of the low-dispersion scheme presented by [23], properly designed for unstable and/or turbulent two-phase flows. The surface tension force, $\mathbf{S}_\sigma$ is transformed to a volume force by using a continuum surface force (CSF) approach, proposed by Brackbill et al. [32], given in formula by

$$\mathbf{S}_\sigma = \sigma \kappa \nabla \phi, \tag{5}$$

where σ is the surface tension coefficient, κ is the curvature and the last term is the gradient of the volume fraction ϕ. The numerical implementation, verification and validation of the surface tension force on our numerical framework is described in [19, 24, 30].

A dynamic mesh refinement strategy is adopted to improve the efficiency of the simulations by increasing the mesh density in areas of the domain where the most important flow structures develop. The Cartesian base mesh undergoes an Octree hierarchical refinement/coarsening process according

to the algorithm proposed by Antepara et al. [20]. Fig. 1(a) represents a basic hexahedron cell of the coarse Cartesian mesh, indicated as level 1, and the sub-cells obtained as a consequence of three progressive refinement stages referred to as level 2, 3 and 4. As an example, Fig. 1(b) shows the inner section of a refined domain, referring to the mesh of the coaxial 3D jet described in Sec. 3.1. The discretization of the refined/coarsened cells accounts for a divergence-free treatment, which ensures the correct transport of mass, momentum and kinetic energy. The process is aimed at ensuring the proper representation of characteristic lengths in each part of the domain, resolving both interfacial and convective scales. In particular, the refinement step is carried out when certain refinement criteria are met over a list of cells. These cells are marked with the corresponding level of refinement during a checking process, performed every certain number of iterations. The refinement criteria used in this work are listed below.

Interface-capturing criterion. It follows the pattern of the level-set function to assign the highest level of refinement in the proximity of the interface, Γ. The refining process is triggered when a minimum number of interfacial control volumes approximates the non-refined domain area. Some additional rings of cells are added to the refined zone, so as to forestall the movement of the fluid and to avoid the process of mesh renewal at each iteration. Departing from Γ, a decreasing level of refinement is assigned, to obtain a smooth transition between highly refined and coarse mesh regions.

Vorticity-based criterion. It is intended to refine the mesh in the zones in which a high vorticity is measured, thus guaranteeing that the smallest scales of the vortices generated by turbulence are well captured. In particular, a specific cell is refined if

$$\frac{\Delta h|\nabla \times \mathbf{u}|}{\max\{\mathbf{u}\}} > \mathbf{\Omega}_{\text{lim}} \tag{6}$$

where Δh is cubic root of the cell volume, and $\mathbf{\Omega}_{lim}$ is a threshold parameter between 0.01 and 0.02.

The inclusion of adaptive-mesh-refinement strategy was tested in past works, demonstrating its effectiveness in the simulation of break-up or general multiphase phenomena [21, 22]. In Schillaci et al. [23] the model is used to carry out the complete simulation of a 2D Coaxial jet in a turbulent scenario.

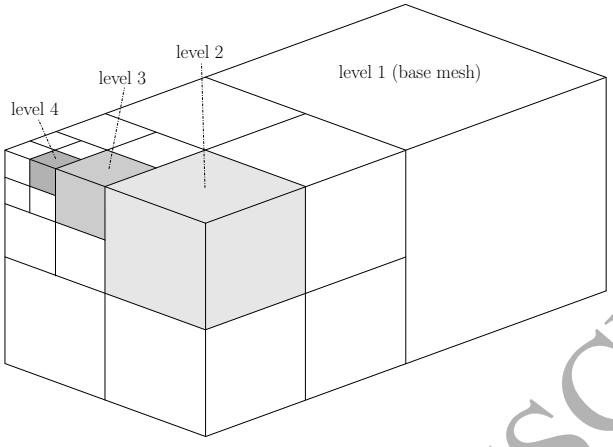

(a)

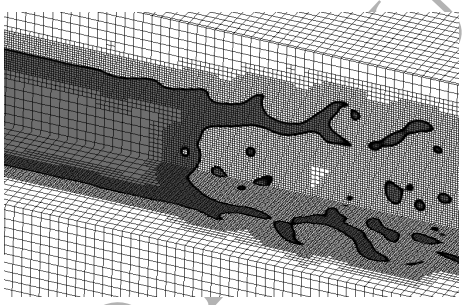

(b)

Figure 1: (a) Octree decomposition of a uniform 3D Cartesian mesh. (b) Inner section of a 3D domain refined with AMR in this work.

3. Validation: the 3D Coaxial Jet Case

The 3D coaxial jet physics, consisting in the parallel injection of two liquid and gas streams, embraces a large range of industrial operations. Some examples are the generation of pharmaceutical sprays or the atomization of liquid propellants in combustion engines. In this section, we describe the results obtained in the numerical simulations of 3D coaxial jets with different properties. The results are compared with semi-empirical correlations found

in experimental literature, thus demonstrating the capability of our numerical framework to carry out the simulation of complex 3D break-up phenomena.

The flow presented in this section is characterized by the Weber number of the gas, We_g, fluid inertia over surface tension ratio, the Reynolds number of the liquid, Re_l, fluid inertia over viscous forces ratio, and the Momentum flux ratio, M, defined as

$$\mathrm{We}_g = \frac{\rho_g u_g^2 h}{\sigma}, \quad \mathrm{Re}_l = \frac{\rho_l u_l D}{\mu_l}, \quad M = \frac{\rho_g u_g^2}{\rho_l u_l^2}. \tag{7}$$

where the subscripts refer to liquid, l, or gas, g, respectively, ρ is the fluid density, μ is the viscosity, σ is the surface tension coefficient, u is the inlet velocity, h is the gas inlet annular gap height and D is the characteristic diameter of the liquid inlet nozzle. The dimensionless time is $t' = tu_l/D$.

In the first proposed case, the *Near-field analysis*, the objective is pointed on the initial destabilization of the jet and its primary break-up. The properties of the involved fluids emphasize the prevalence of aerodynamic forces, thus allowing a clear identification of the instabilities that lead to liquid core rupture, i.e. Kelvin-Helmholtz (KH) and Rayleigh-Taylor (RT) instabilities. In the second test, identified as *Far-field analysis*, the secondary atomization process is studied more in detail by setting a longer domain length. Hence, particular attention is given to the measurement of the diameter of the droplets resulting from the atomization process.

The atomization of a liquid jet by means of a fast parallel gas stream

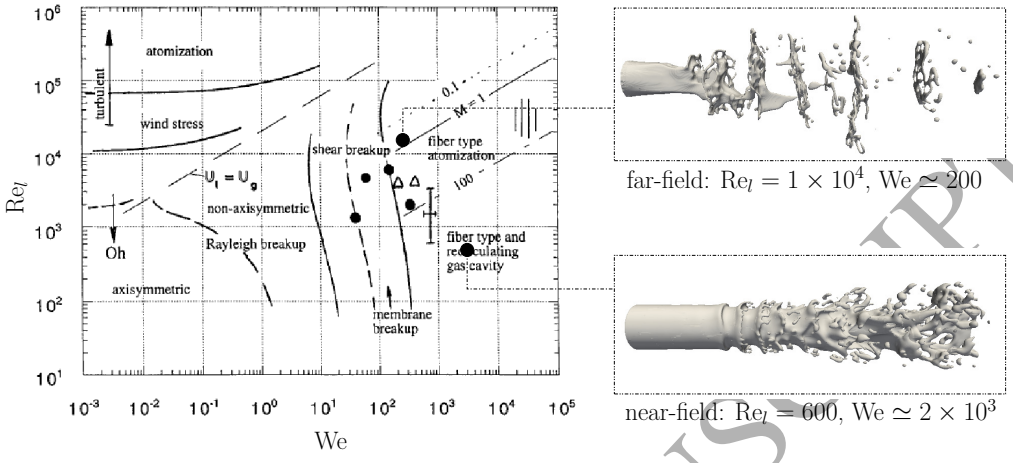

Figure 2: Break-up regime diagram of coaxial jets extracted from [26], function of Re_l and We= $\rho_g u_g^2 D_l/\sigma$ parameters. M= $\rho_g u_g^2/\rho_l u_l^2$ is the momentum flux ratio. On the right, a graphical resume of the cases analyzed in this work is depicted.

has been analyzed experimentally by several authors, such as Marmottant and Villermaux [27], Varga et al. [33], Rayana et al. [34]. Their works provide semi-empirical correlations for the calculation of characteristic amplitudes, valid for a specific range of physical conditions and set-up features of the coaxial jet. In the following part of this section, simulations are validated by comparing the characteristic amplitudes these reference values. The magnitudes considered are the wavelength of the KH instability, λ_{KH}, the Rayleigh-Taylor wavelength, λ_{RT}, the intact jet length, L/D, and the Sauter mean diameter of droplets, d_{32}.

3.1. Near-field analysis

In this paragraph, we propose the simulation of a coaxial jet with $\mathrm{Re}_l = 600$ and $\mathrm{We}_g = 4.5 \times 10^3$. Given the predominance of aerodynamic forces

	Re_l	We_g	CVs
near-field	600	4500	2.5×10^6
far-field	9980	204	6.6×10^6

Table 1: 3D Coaxial Jet: dimensionless numbers and CVs at steady state.

Test	SPC	CPUs	CVs	time [h×CPU]
near-field	JFF [35]	128	∼2.5M	∼720
far-field	Finisterrae II [36]	512	∼6.5M	∼500

Table 2: Coaxial Jets: computational details of the simulations. SPC is the employed supercomputer, together with the related number of CPUs; CVs is the averaged number of dynamic cells involved in the simulations while the time indicates the number of hour (per CPU) for which the case was run.

and the short length of the domain, this case is thought to show in detail the phases of the destabilization process that lead to primary break-up. The numerical set-up, depicted in Fig. 3, consists of a rectangular box, in which a high-speed round liquid jet, with diameter D, is injected at constant horizontal velocity. The box has dimensions $9D \times 3D \times 3D$. The coaxial gas flux flows from the outer gap of amplitude $h \simeq 2D$. Dimensionless numbers are reported in Tab. 1 (near-field case). At the other boundaries an outflow pressure based condition is applied. A lv.3 AMR is used on a basic mesh of $\sim 3.5 \times 10^5$ cells. At statistical steady state, the mesh counts $\sim 2.5 \times 10^6$ elements, and $(\mathrm{D}/\Delta h)_{\mathrm{lv.3}} = 60$. Alternatively, the achievement of the same resolution on a static Cartesian mesh would require the employment of $\sim 2.1 \times 10^7$ elements. More details above computational data are given in Tab. 2.

According to the break-up regime diagram proposed by Lasheras and Hopfinger [26], and reproduced in Fig. 2, the flow properties indicate a fiber type atomization regime. In Fig. 3, a screenshot of the completely developed coaxial jet is also reported. In the zoom one can observe in detail the Kelvin-Helmholtz mechanism, characterized by the KH instability wavelength, λ_{KH}. This instability is due to the shear stress appearing between two parallel streams flowing with different velocities. The interfacial fluctuations cause the appearance of waves that quickly grow, amplify and roll-up. In the case of an axial liquid injection, perturbed by a parallel laminar gas flow, λ_{KH} can be evaluated by using the formulation proposed by Marmottant and Villermaux [27]. They state that, in case of high We number, the wavelength is proportional to the vorticity layer thickness, δ, and it may be evaluated as

$$\lambda_{\mathrm{KH,mar}} \simeq C\sqrt{\frac{\rho_l}{\rho_g}}\delta, \tag{8}$$

with constant $C \simeq 1.2$ for the coaxial axisymmetric configuration. In the case of laminar flow inlet, the vorticity layer thickness can be evaluated as $\delta = 5.6h/\mathrm{Re}_g$, where h is the air-gap inlet length. Numerical values for λ_{KH}/D, are evaluated from a graphical analysis of the jet pictures and compared to the semi-empirical correlations, being $(\lambda_{\mathrm{KH}}/D)_{\mathrm{num}} \simeq 0.37$. Good agreement is found with the reference value, $(\lambda_{\mathrm{KH}}/D)_{\mathrm{ref}} \simeq 0.43$, evaluated according to Eq. 8. Results are reported in Tab. 3.

The acceleration of the liquid surface due to the KH instability is the

triggering for the further destabilization of the flow. Indeed, the accelerated crest of the waves generated by the first instability, developing on a direction perpendicular to the main flow, are subjected to a Rayleigh-Taylor (transverse) type instability. This consists in the action of the light phase pushing on the heavier one, causing the appearance of ligaments on the top of the wave crests. This phenomenon, characterized by λ_{RT} wavelength, is also highlighted in the zoom of Fig. 3. [27] proposes a correlation for the evaluation of λ_{RT}, expressed as

$$\lambda_{\mathrm{RT,mar}} \simeq 2.8\delta \mathrm{We}_{\delta}^{-1/3} \left(\frac{\rho_g}{\rho_l}\right)^{-1/3}, \tag{9}$$

where We_{δ} is the Weber number of the vorticity layer, evaluated as $\mathrm{We}_{\delta} = \rho_g u_g^2 \delta/\sigma$. Again, good agreement is found between the numerical value, $(\lambda_{\mathrm{RT}}/D)_{\mathrm{num}} \simeq 0.14$, and the experimental one, $(\lambda_{\mathrm{RT}}/D)_{\mathrm{ref}} \simeq 0.11$, evaluated from Eq. 9.

Altogether, the two instability mechanisms described form the primary break-up process. Following, the amplification of the disturbances downstream leads to the fragmentation of the liquid core and the spreading of droplets downstream. The complete break-up of the liquid core occurs at some liquid-jet diameters from the injection. Some authors have analyzed the mean liquid-core intact length, L/D, e.g. Lasheras and Hopfinger [26]

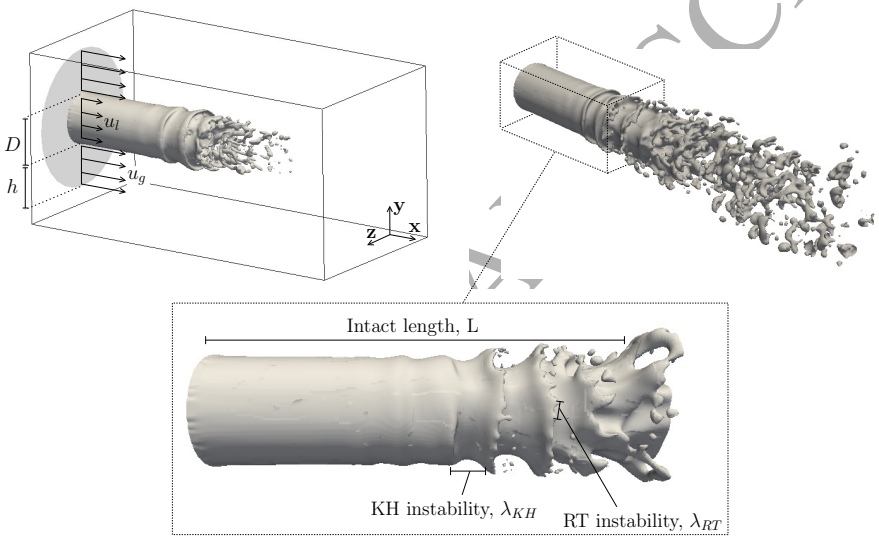

Figure 3: 3D Coaxial Jet: near-field analysis of the jet ($\mathrm{Re}_l = 600$, $\mathrm{We}_g = 4.5 \times 10^3$). On the top-left, the numerical set-up is depicted. In the top-right screenshot ($t' = 6.3$), the jet surface is first unstabilized by waves, that successively roll-up causing primary atomization. In the zoom, the instability wavelengths λ_{KH}/D and λ_{RT}/D and the intact length of the jet, L/D, are indicated.

	λ_{KH}/D		λ_{RT}/D		L/D		$d_{32}[\mu\mathrm{m}]$	
	num.	ref.	num.	ref.	num.	ref.	num.	ref.
near-field	0.37	0.43	0.14	0.11	4.66	4.75	-	-
far-field	-	1.26	-	0.49	4	5	1180	1377

Table 3: 3D Coaxial Jet: characteristic lengths measured in simulations (num.) and comparison to experimental data (exp.) by [27] and [26].

provide a general expression that reads as

$$\frac{L}{D} \simeq \frac{6}{\sqrt{M}} \left(1 - \frac{u_l}{u_g}\right)^{-1}. \tag{10}$$

The numerical value for the intact-length of the jet, L/D, is well captured, as $(L/D)_{\mathrm{num}} \simeq 4.66$ acceptably matches the experimental data, $(L/D)_{\mathrm{ref}} \simeq 4.75$, expressed by Eq. 10. The droplet size is not analyzed in this case as the test was focused on the near-field of the jet and the path traveled by particles is not long enough to show a complete disintegration.

3.2. Far-field analysis

In the second test, a longer and wider domain is adopted ($15D \times 5D \times 5D$). It allows a better analysis of the far-field, where the liquid core is totally broken and the structures resulting from primary break-up have mostly degraded into droplets. The numerical set-up reflects the one used in the near-field analysis, while the new properties are highlighted by dimensionless numbers in Tab. 1. $\mathrm{Re}_l \simeq 1 \times 10^4$ and $\mathrm{We}_g \simeq 200$, indicate a fiber type atomization regime closer to the turbulent zone. At statistical steady state, the mesh is characterized by a dynamic definition of $(D/\Delta h)_{\mathrm{lv.3}} = 72$. The

minimum definition is set as a result of preliminary tests, and it is aimed at guaranteeing the maximum reduction of numerical coalescence between the particles generated by the primary break-up. Further details above computational resources are given in Tab. 2.

An overview of the flow evolution is presented in Fig. 4. The absence of a predominant action of the aerodynamic forces in the near-field zone makes the visual identification of the initial instabilities that lead to the core breakdown, λ_{KH} and λ_{RT}, more difficult. Indeed, the instabilities present a large temporal variability and appear partially overlapped. Furthermore, the low Weber number, We_g, indicates a decrease in the efficiency of the aerodynamic forces in the generation of surface waves. Due to the fact that the instabilities are not clearly distinguished (as in the near-field analysis), their wavelengths are not measured in this case. Once ligaments are generated by the transverse instability, they quickly degenerate into droplets, and their size is demonstrated to be proportional to the wavelength of the transverse instability [27, 33, 34]. The latter is much smaller than the axisymmetric (Kelvin-Helmholtz) wavelength. Experimental works demonstrated the existence of a proportionality correlation between the mean droplet size in the atomized region and λ_{RT}, e.g. [27] states that the Droplet Mean Diameter, d_{32}, can be found as

$$d_{32,\mathrm{mar}} \simeq 0.28\lambda_{\mathrm{RT,mar}}. \tag{11}$$

In our simulations, the characteristics of the droplets cloud is studied by

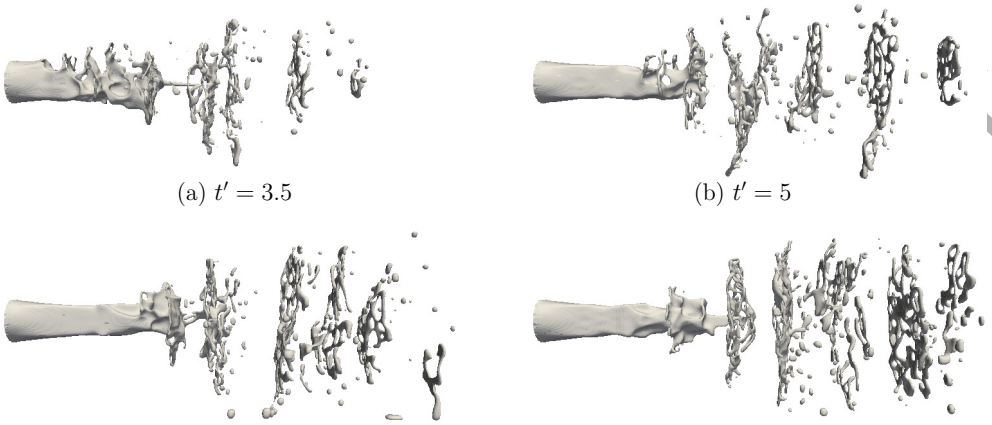

(a) $t' = 3.5$ (b) $t' = 5$

(c) $t' = 6.5$ (d) $t' = 8$

Figure 4: 3D Coaxial Jet: snapshots of the jet simulated in the far-field analysis ($\mathrm{Re}_l \simeq 1 \times 10^4$, $\mathrm{We}_g \simeq 200$).

analyzing the zone of the domain where, after a few diameter lengths, x/D, the presence of droplets is stable. The analysis is carried out by means of an image treatment which allows the recognition of the diameter of the droplets that pass through a given section. The distribution of the drops presents a fairly regular normal shape after a certain distance from the origin, $x/D \simeq 6$. A statistical analysis allows the identification of the Sauter Mean Diameter, d_{32}, to be compared with reference data. The measured value for $(d_{32})_{\mathrm{num}} \simeq 1180$ μm agrees well with reference value, $(d_{32})_{\mathrm{num}} \simeq 1377$ μm, evaluated with Eq. 11 [27].

Finally, the liquid core intact-length, $(L/D)_{\mathrm{num}} \simeq 4$, despite being slightly sub-estimated, is in good agreement with the reference value by [26], $(L/D)_{\mathrm{ref}} \simeq 5$, expressed by Eq. 10.

4. Liquid Injection: a Review of Atomization Regimes

The principal scope of this work is to propose a complete break-up regime map of the liquid jet set-up, consisting in the injection of a high-velocity fluid inside a still air chamber. Differently from Sec. 3, the dimensionless numbers for this case are defined as function of the inlet liquid velocity, u_l, being the inlet gas velocity equal to 0. Hence, the characteristic parameters, We_g, and Re_l are defined as

$$\mathrm{We}_g = \frac{\rho_g u_l^2 D}{\sigma}, \quad \mathrm{Re}_l = \frac{\rho_l u_l D}{\mu_l}, \tag{12}$$

respectively. The other fundamental parameter is the Ohnesorge number

$$\mathrm{Oh} = \frac{\mu_l}{\sqrt{\rho_l \sigma D}}, \tag{13}$$

defined as the ratio between viscous forces, which tend to keep the flow stable, and the product of inertia and surface tension which tend to break the liquid surface. As reported by various authors [17, 37, 38], the dispersion pattern of a liquid jet mainly depends on Re_l and Oh parameters. By maintaining the fluids properties fixed, the most universally recognized regimes can be obtained by progressively increasing the inlet mass flow rate, as described below.

In the *dripping regime*, the liquid drops are directly emitted at the nozzle exit. This regime is characterized by a very low value of u_l.

When a laminar liquid is injected at low velocity (*Rayleigh regime*), it forms a ligament that degenerates into droplets. These drops have a charac-

teristic diameter, d_{drop}, in the order of magnitude of the inlet jet diameter, D. This phenomenon, similar to the dripping of water from a tap, is due to the axisymmetric propagation of Rayleigh –or dilatational waves, and it is driven by surface tension forces. This regime is the first characterized by a break-up length, or intact-length of the jet, L, defined as the length at which the rupture of the ligament occurs, or, alternatively, as the length of the intact jet attached to the nozzle.

For higher Reynolds number (wind-Induced regime), the inertial forces assume greater importance. The jet develops asymmetric instabilities, and releases small droplets, $d_{\text{drop}} < D$. The intact length of the jet initially increases with the velocity, but it starts to recede once a limit Re number has been reached [39]. Some authors as Dumouchel [38] distinguish between *first* and *second wind-induced regime*. In the first wind-induced regime there is a dominant perturbation evolving on the jet interface, which, although showing mixed asymmetric/axisymmetric characteristics, does not produce organized drops as in the Rayleigh regime. The drop-size distribution may become wider, but the diameters are still in the order of magnitude of the jet diameter. On the other side, in the second wind-induced regime the jet column shows a more disturbed shape and different length scales of the growing perturbations. Droplets are generated firstly by a peeling-off of the interface and, secondly, from the rupture of the liquid core. The large structure that may results from the core break-up may still undergo secondary atomization.

For stronger flow rates (Atomization regime), the aerodynamic effects

become dominant and the jet undergoes a total atomization close to the inlet. The final size of the droplets —generated by both primary and secondary break-up processes— span over a wide range of scales, and is defined by means of a statistical value ($d_{\mathrm{SMD,drop}} << D$).

A common way used to characterize the disintegration mechanism consists in the study of the break-up length as function of the inlet velocity. A typical L versus u_l plot is shown in Fig. 5(a), extracted from Reitz and Bracco [40]. This plot shows how —as explained before— L initially increases with the velocity, but it reaches a peak and starts to diminish when aerodynamic forces increase their importance. When entering in the second wind-induced regime, there still remain some confusion over the true shape of the curve: some authors state that the break length remains constant [17], while others as [41, 38] suggest that it may initially increase again. It should be noted that the definition and measurement of the intact length in the most chaotic regimes become more difficult. For these cases, it is helpful to define two different break-up length: the intact-surface length, L_s, indicates the minimum distance at which particles begin to be disrupted from the jet surface; the intact-core length, L or L_c, indicates the length for the complete disintegration of the liquid core. The two lengths coincide in Rayleigh and first wind-induced regime, but become different in the second wind-induced, as the disruption of the jet-surface starts to generate primary droplets. According to Reitz and Bracco [40], the atomization regime is characterized by the fact the L_s is always zero, while the rupture of the core still occurs at a

certain distance, L_c, from the inlet.

Several authors have tried to delimit the various regions by means of dimensionless value correlations, usually involving We_l, We_g, Re_l and Oh numbers.The most commonly used correlations that delimit the various regimes are listed as follows.

- From dripping to Rayleigh regime: as stated by Ranz [42], the dripping from the nozzle no longer occurs if the liquid inertia overcomes surface tension constraining forces. This happens when

$$\mathrm{We}_{l,\mathrm{lim}} > 8 \tag{14}$$

- From Rayleigh to first wind-induced regime: the limit comes from linear stability theorem considerations, and, as expressed by Sterling and Sleicher [43], it can be written as

$$\mathrm{We}_{g,\mathrm{lim}} > 1.2 + 3.41\mathrm{Oh}^{0.9} \tag{15}$$

- From first to second wind-induced regime: the same Ranz [42] argued that this transition occurs when gas inertia forces reach the magnitude of surface tension forces. This is expressed by

$$\mathrm{We}_{g,\mathrm{lim}} > 13 \tag{16}$$

- From wind-induced to atomization regime: the criterion, provided by Miesse [44], comes from empirical considerations, stating that transition occurs when

$$\mathrm{We}_{g,\mathrm{lim}} > 40.3 \tag{17}$$

The limit Weber numbers are plotted on the spray break-up regimes (function of We_g and Oh) provided by Faeth [37], and shown in Fig. 5(b). However, these correlations are not taking into account the role of liquid viscosity. In Reitz and Bracco [40], the jet break-up regimes are represented as function of Re_l and Oh parameters. As pointed out by the same authors, the plot does not take into account the effect of gas density or the initial turbulence of the jet. This demonstrates that satisfactory correlations for the regime boundaries are not still available, and that more results from experimental, and, maybe, numerical works are needed to obtain a complete knowledge of the considered phenomena.

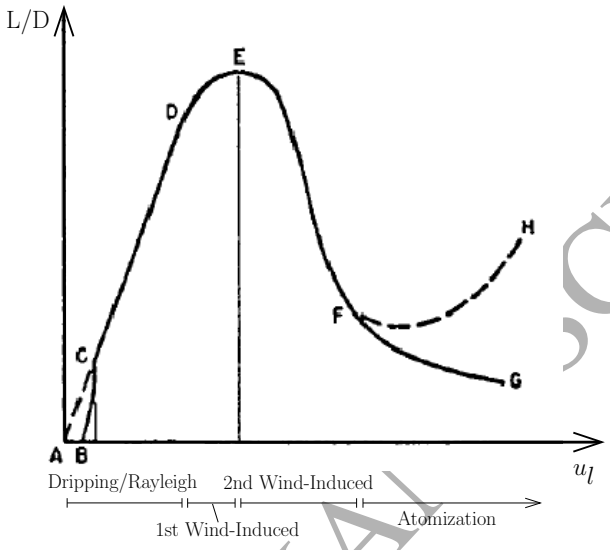

(a)

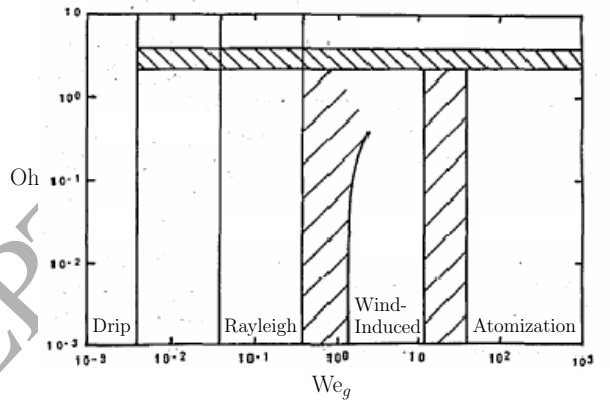

(b)

Figure 5: (a) Jet break-up length as function of the inlet liquid velocity, adapted from Reitz and Bracco [40]. (b) Break-up regime map as function of We_g and Oh dimensionless numbers, extracted from Faeth [37].

5. Liquid injection: Numerical Simulations

In this section we perform a series of simulations aimed at studying the variability of the jet characteristics as function of selected input parameters. In particular, the analyzed variables are Re_l, Oh and We_g. We will compare the pattern obtained in simulations with the one expected from bibliographic study, situating each case on a break-up regime map. The simulations were carried out on the JFF and on Mare Nostrum IV [45] supercomputers by employing from 64 to 384 CPUs during 3 to 10 days of simulation to reach a statistical steady-state.

5.1. Numerical Set-up

The problem consists in the injection of a high-speed stream of liquid l into a rectangular box filled by quiescent gas g. The numerical set-up, depicted in Fig. 6, consists of a rectangular box, where a fluid jet of diameter $D = 4.5 \times 10^{-5}$ and velocity u_l is injected with constant stream-wise velocities starting from the left boundary of the domain. The rectangular box used has variable dimensions to adapt to the type of structures developed by the jet. It reaches the maximum size of $60D \times 15D \times 15D$ in cases where the jet develops considerably both in radial and frontal direction, e.g. Tests 6–8. An outlet pressure is imposed at the other boundaries in order to represent the outflow conditions. The properties of the fluids are specified in each section.

The base mesh is a uniform Cartesian grid, subjected to a progressive refinement in the sub-domains where small characteristic lengths have to

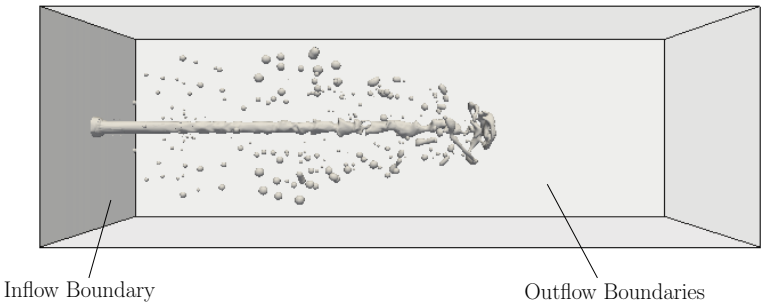

Figure 6: Numerical set-up used in this work for the simulation of the liquid injection.

Mesh	$\Delta h_{\mathrm{lv.1}}$	$\Delta h_{\mathrm{lv.3}}$
mesh A	1.0×10^{-5}	2.5×10^{-6}
mesh B	7.0×10^{-6}	1.75×10^{-6}

Table 4: Characteristics of the meshes used in the simulations. The characteristic length of the base mesh, $\Delta h_{\mathrm{lv.1}}$, and the minimum length reachable by means of the dynamic mesh strategy, $\Delta h_{\mathrm{lv.3}}$, are indicated.

be represented. In the considered test, a maximum level 3 refinement is utilized, i.e. the parent cell is divided into maximum 64 sub-cells. Two different base meshes are used in the tests, whose characteristic lengths are described in Tab. 4. The choice of the mesh follows a convergence study aimed at verifying the influence of the mesh size on the magnitude of some characteristic quantities, i.e. the break-up length or the size of the drops.

5.2. Study of inlet velocity variation

In the tests reported in this section we describe the behavior of jets with increasing inlet velocity, u_l, in order to analyze the transition between break-up regimes. The Oh number is kept constant in the experiments, while

constantly increasing Re_l and We_g. The properties of the fluids employed in the simulations are highlighted in Tab. 5, corresponding to the ones of water dispersed into carbon dioxide at 308 K and 60 bar. A summary of the dimensionless numbers used in the simulations is reported in Tab. 6. The approximate number of cells at steady-state is indicated in Tab. 6. Figs. 8 to 15 are intended to show the behavior of the different jets during the initial transition phase and at steady-state. The single tests are described as follows.

- In Fig. 8 some screenshots of the flow simulated in Test 1 —characterized by Re_l=136— are reported, as function of dimensionless time $t' = tu_l/D$. As a characteristic feature of the Rayleigh regime, the jet releases droplets with the order of magnitude of its diameter. The average break-up length, varies in the range of $L/D \simeq 15.8$. Some droplets then merge downstream, creating bigger leading drops.

- In Test 2, in which the input speed of the liquid is higher (Re_l=193), $L/D \simeq 19.2$ is longer than in the previous case. This is consistent with the behavior of jets in the Rayleigh regime [37], whose pinch-off length become longer with the increase of jet velocity. We also noticed a smaller diameter of the released droplets, and a less relevant downstream merging process, as shown in Fig. 9.

- The same pattern is observed in Test 3, as depicted in Fig. 10, characterized by a slightly longer break-up length, $L/D \simeq 24$.

- In Test 4, characterized by Re_l=386, one can observe how the growth

of instability is no longer exclusively axisymmetrical, highlighting an increasing influence of shear stresses as responsible for the jet break-up. As mentioned in Sec. 4, this indicates the passage of the jet to the wind-induced regime. Moreover, the release of droplets from the tip of the jet becomes irregular, as shown in the screenshots of Fig. 11. The intact length of the jet results increased also in this case, $L/D \simeq 26.7$.

- The effect of a slight increase in inlet velocity compared to Test 4 causes a further lengthening of the break-up length, which shows the maximum value, $L/D \simeq 38.9$, in Test 5, corresponding to Re_l=511. The break-up mechanism maintains the characteristic of the first wind-induced regime, as depicted in Fig. 12.

- In Test 6 (Fig. 13), with Re_l=1022, the jet is still characterized by the growth of non-symmetrical instabilities as characteristic of the wind-induced regime, and the irregular rupture of the ligament occurs at $L/D \simeq 21.7$. However, we can observe a higher peeling-off of droplets from the jet surface by comparison to Tests 4 and 5, which is evidence of the positioning of Test 6 within the second wind-induced regime range. As reported in Tab. 6, the important rise of CVs in the simulations is due to the necessity of adopting a finer base mesh (mesh B), to correctly capture the features of the flow.

- In Test 7, the scenario changes again, as demonstrated by screenshots of Fig. 14, marking a clear passage from the wind-induced to the atom-

ization regime. The liquid column is quickly made unstable by asymmetrical perturbations, which lead to the rapid and violent breakage of the core. The liquid then disperses in a myriad of small particles, whose diameter distribution can be studied through a statistical study and expressed as a function of a mean diameter and a variance. The intact length is subjected to a strong retreat, as it fluctuates around $L/D \simeq 17$. The number of dynamic CVs needed to represent the flow at steady-state reaches $\sim 1.2 \times 10^7$.

- A stronger atomization pattern is observed in Test 8 (Re_l=2045), characterized by a finer dispersion of particles by respect to Test 6. Some screenshots of the flow are reported in Fig. 15, where the intact length results stabilized around $L/D \simeq 13.3$.

Tests 1–5 were run on JFF cluster, while Tests 6–8 were launched on MareNostrum IV supercomputer, in order to overcome the large memory and CPU requirements necessary to deal with a huge mesh made of dynamic elements. In Tab. 7, we report some details on computation time and statistics.

In the cases belonging to the Atomization regime, Tests 7 and 8, we measured the size of the small droplets resulting from the disruption of the core, adopting the method already described in Sec. 3.2. The size of the drops has been measured in different sections of the domain, and the variation of d_{mean}/D along the x coordinate is reported in Fig. 7. The measurement is

Mesh	liquid, l	gas, g
ρ [kg/s]	994	163
μ [Pa·s]	7.42×10^{-4}	1.92×10^{-5}
σ [N/m]	0.0742	

Table 5: Study of inlet velocity variation: fluid properties employed in the simulations.

possible after a certain interval from the core breaking. In particular, the mean particle size was measured starting from sections $x/D = 25 : 30$, where the full rupture of the structures and a homogeneous disintegration after the core break-up zone has already occurred. Thus, in both cases an initial diameter reduction can be noted, followed by a progressive increase in the far-field. This behavior can be explained by taking into account the competition between break-up tendencies and coalescence effects, as also noticed by past authors [26, 46]. The diameter of the drops measured in the sector of minimum size ($x/D = 40 : 55$), is reported in Tab. 8. As expected from the finer atomization pattern, Test 8 shows a slightly smaller value of d_{mean}/D than Test 7.

5.3. Intact length analysis

As explained in Sec. 4, the analysis of the variation of the break-up length with the inlet liquid speed, constitutes a qualitative verification of the jet study. In this work, L/D was evaluated by measuring the break-up point of the liquid core on several flow screenshots, once the statistical steady state was reached. Therefore, the values presented here are found by performing an average of the collected numerical measurements. As shown in Fig. 16,

	Re_l	We_g	Oh	L/D	CVs
Test 1 (T1)	136	0.5	0.013	~ 15.8	3.6×10^6
Test 2 (T2)	193	1.0	0.013	~ 19.2	3.4×10^6
Test 3 (T3)	253	1.7	0.013	~ 24	3.8×10^6
Test 4 (T4)	386	4.0	0.013	~ 26.7	3.4×10^6
Test 5 (T5)	511	7.1	0.013	~ 38.9	4.3×10^6
Test 6 (T6)	1022	28.4	0.013	~ 21.7	7.3×10^6
Test 7 (T7)	1500	61.2	0.013	~ 17	9.8×10^6
Test 8 (T8)	2045	113.7	0.013	~ 13.3	1.2×10^7

Table 6: Liquid Jet: dimensionless numbers of the injected liquid and intact length of the jet. The approximate number of CVs is also indicated.

	Re_l	CPUs	CVs	t/t'_{end} [h×CPU]
Test 6	1022	288	7.3×10^6	2.1
Test 7	1500	336	9.8×10^6	2.3
Test 8	2045	384	1.2×10^7	2.2

Table 7: Liquid Injection: computational details of the simulations run on MareNostrum IV supercomputer, together with the related number of CPUs employed. CVs is the averaged number of dynamic cells at steady state, while t/t'_{end} indicates the number of hour (per CPU) needed to simulate a dimensionless time unit of the case.

	Re_l	$\mathrm{d}_{\mathrm{mean}}/\mathrm{D}$
Test 7	1500	~ 0.2
Test 8	2045	~ 0.17

Table 8: Liquid Injection: mean size of the particles measured in the Atomization regime.

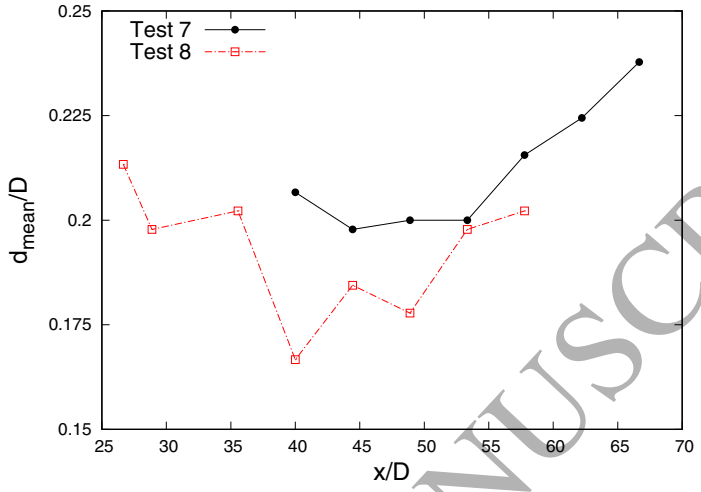

Figure 7: Liquid Injection: mean drop size, d_{mean}/D, in different sections of the domain. The measurement is carried out for Atomization cases, Tests 7 and 8, at different distances, x/D, from the liquid inlet.

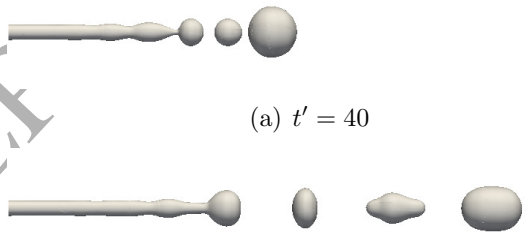

(a) $t' = 40$

(b) $t' = 100$

Figure 8: Liquid Jet (T1): screenshots of the flow characterized by $\text{Re}_l = 136$. Dripping/Rayleigh regime.

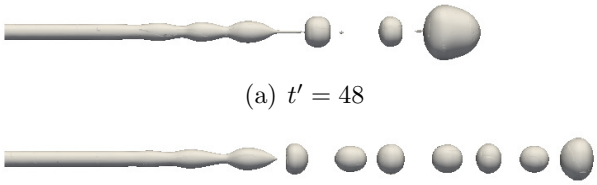

(a) $t' = 48$

(b) $t' = 93$

Figure 9: Liquid Jet (T2): screenshots of the flow characterized by $\mathrm{Re}_l = 193$. Rayleigh regime.

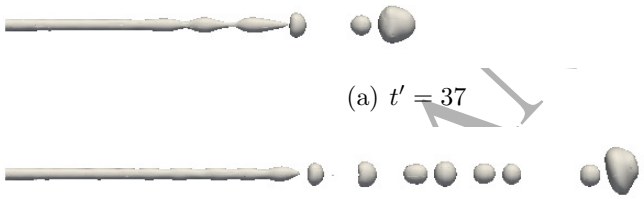

(a) $t' = 37$

(b) $t' = 60$

Figure 10: Liquid Jet (T3): screenshots of the flow characterized by $\mathrm{Re}_l = 253$. Rayleigh regime.

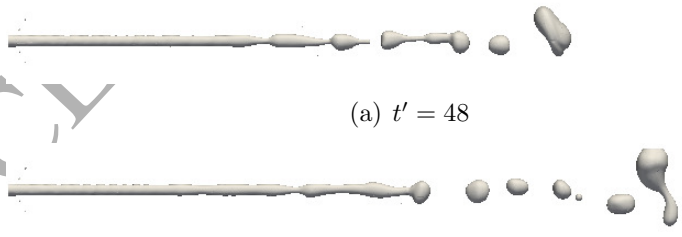

(a) $t' = 48$

(b) $t' = 60$

Figure 11: Liquid Jet (T4): screenshots of the flow characterized by $\mathrm{Re}_l = 386$. First Wind-Induced regime.

(a) $t' = 75$

(b) $t' = 105$

Figure 12: Liquid Jet (T5): screenshots of the flow characterized by $\mathrm{Re}_l = 511$. First Wind-Induced regime.

(a) $t' = 38$

(b) $t' = 53$

Figure 13: Liquid Jet (T6): screenshots of the flow characterized by $\mathrm{Re}_l = 1022$. Second Wind-Induced regime.

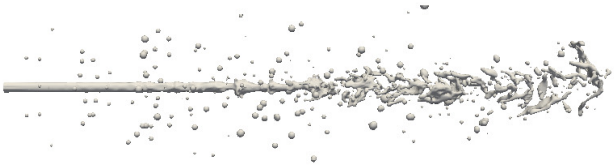

(a) $t' = 75$

(b) $t' = 117$

Figure 14: Liquid Jet (T7): screenshots of the flow characterized by $\mathrm{Re}_l = 1500$. Atomization regime.

(a) $t' = 75$

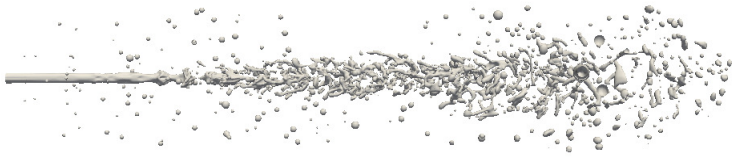

(b) $t' = 117$

Figure 15: Liquid Jet (T8): screenshots of the flow characterized by $\mathrm{Re}_l = 2045$. Atomization regime.

which represents the trend of the dimensionless value of L as a function of Re_l, L/D increments initially, passing from the Rayleigh regime to the first-wind induced one. Subsequently, it undergoes a reduction in the transition from wind-induced to atomization; then it stabilizes to a nearly constant value. The graph shows the trend of the same magnitude measured in the experimental work of Badens et al. [17]. In the increasing part of the function we can see a remarkable similarity between the results. The maximum value of L/D found by Badens et al., corresponds to the case at $\mathrm{Re}_l = 566$, while in our study it corresponds to $\mathrm{Re}_l = 511$. The two lengths are very close, being the experimental value of Badens equal to $(L/D)_{\mathrm{Bad.,max}} = 37.5$ against an $(L/D)_{\mathrm{max}} = 38.9$ found in our study. On the other hand, in the decreasing part of the function we can see a certain discrepancy between the results. Indeed, for $\mathrm{Re}_l > 700$, L/D measured by Badens et al. results shorter than in our simulations. This is probably due to a difference in the inlet velocity profile between the numerical cases and the experiments. In fact, at intermediate-high Reynolds number, the experimental jet evolution may be affected by the lateral fluctuations present in the inlet velocity profile, due to the influence of the mechanical injector. These perturbations lead, in conjunction with the prevalent aerodynamic forces, to an earlier instability of the jet, and consequently to a shorter break-up length. On the other hand, the inlet profile imposed in the simulations is regular for all the Reynolds number, without the introduction of any additional disturbance that would fasten the core rupture. Finally, the minimum value for the intact length

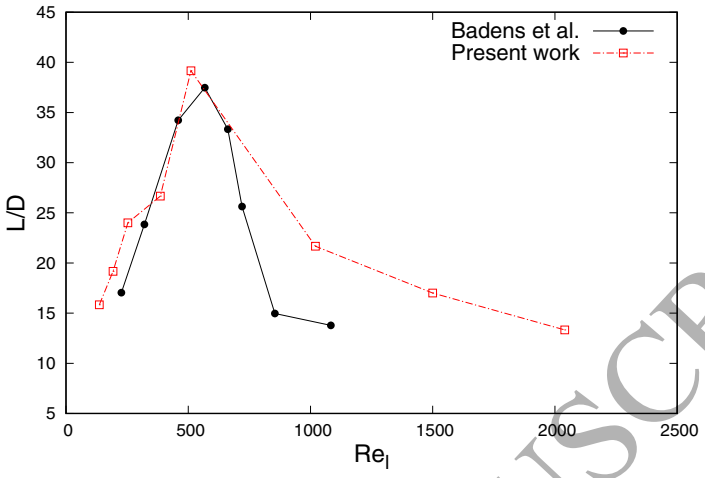

Figure 16: Liquid Injection: variation of the dimensionless break-up length of the jet as a function of the inlet Reynolds number, Re_l. The behavior obtained in our simulations is plotted together with the one obtained by Badens et al. [17] in their experimental work.

found in our work, $(L/D)_{\mathrm{min}} = 13.3$ (at $\mathrm{Re}_l = 2045$), is very close to that of Badens, $(L/D)_{\mathrm{Bad.,min}} = 13.7$ (at $\mathrm{Re}_l = 1083$).

5.4. Effect of surface tension coefficient

In this section the effect of varying the surface tension coefficient on the jet dynamics is analyzed and commented. Some of the previous cases (Tests 2, 5 and 6) are repeated using a lower surface tension value. This effect causes an increase in the Ohnesorge and We_g numbers, and consequently a stronger tendency of the structure to break under the effect of perturbations. The cases analyzed are resumed in Tab. 10, while the fluid properties are highlighted in Tab. 9. Respectively, we can notice the following transitions.

- Test 2–b, the regime has passed from the pure Rayleigh of Test 2 to a wind-induced one, between first and second, characterized by the rise

Mesh	liquid, l	gas, g
ρ [kg/s]	994	163
μ [Pa·s]	7.42×10^{-4}	1.92×10^{-5}
σ [N/m]	0.024	

Table 9: Effect of surface tension: fluid properties employed in the simulations.

	Re_l	We_g	Oh
Test 2	193	1.7	0.0129
Test 2–b (T2–b)	193	3.13	0.023
Test 5	511	7.1	0.0129
Test 5–b (T5–b)	511	22	0.023
Test 6	1022	28.4	0.0129
Test 6–b (T6–b)	1022	88	0.023

Table 10: Liquid Jet: parameters of the simulations in the series of variable Oh number.

of non-symmetrical instabilities (Fig. 17) and a longer break-up length. The peeling-off of droplets indicates a closer proximity to the second wind-induced regime.

- In Test 5–b, depicted in Fig. 18, we can see a stronger peeling-off of droplets compared to Test 5, thus indicating the passage from first to second wind-induced regime.

- In Test 6–b, the regime has clearly passed from the wind-induced case of Test 6 to atomization, as indicated by the sustained disintegration of structures shown in Fig. 19. Moreover, the break-up length results substantially reduced.

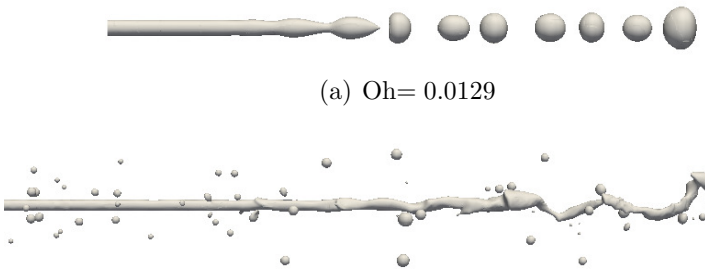

(a) Oh= 0.0129

(b) Oh= 0.023

Figure 17: Water Jet: $\mathrm{Re}_l = 193$, effect of the surface tension increase (Test 2 and Test 2–b). The pictures refer approximately to the same t^*.

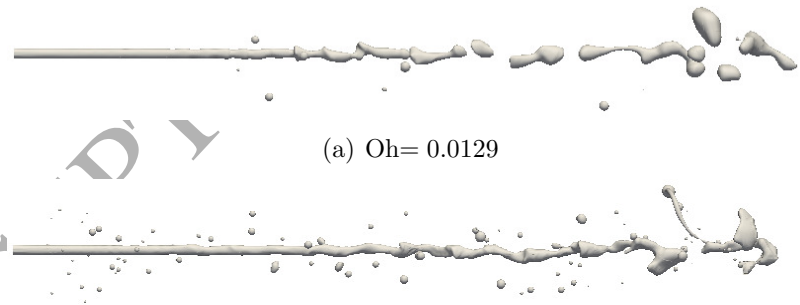

(a) Oh= 0.0129

(b) Oh= 0.023

Figure 18: Water Jet: $\mathrm{Re}_l = 511$, effect of the surface tension increase (Test 5 and Test 5–b). The pictures refer approximately to the same t^*.

(a) Oh= 0.0129

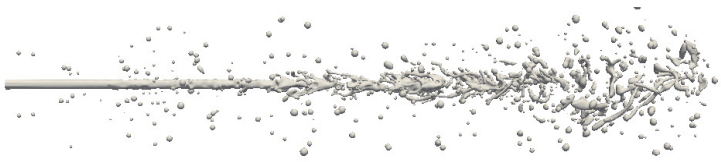

(b) Oh= 0.023

Figure 19: Water Jet: $\mathrm{Re}_l = 1022$, effect of the surface tension increase (Test 6 and Test 6 –b). The pictures refer approximately to the same t^*.

5.5. Liquid Injection: Atomization Map

In this paragraph, all the tests analyzed in Sec. 5 are collected and classified as function of dimensionless parameters; in particular, We_g versus Oh, and Re_l versus Oh. The scope is to compare the patterns found in numerical experiments with the ones dictated by the theoretical and empirical correlations found in literature for the identification of the disintegration regimes.

As explained in Sec. 4, the limit between the regimes are usually described by characteristic Weber numbers, indicated by the black vertical lines in the We_g vs. Oh plot, shown in Fig. 20. Given the physical properties of the fluids used in the tests, we can also plot the characteristic lines on the Re_l vs. Oh chart, reported in Fig. 21. In the same plots we have reported, together with the black lines indicating the correlations taken from literature, three red lines

representing the approximate transition zones observed in our simulations. From the analysis of the break-up and atomization patterns observed in the study of the inlet velocity variation (Sec. 5.2) and in the variable surface tension series (Sec. 5.4), we have obtained the information reported below.

Tests 1 and 2 lie in their proper range, being both pure Rayleigh break-up cases. Instead, Test 3 still lies inside the Rayleigh regime range, while expected to fall within the first wind-induced zone according to the literature. Finally, Test 2–b lies in 1°W.I., respecting the positioning marked by the reference line. Hence, in the transition between Rayleigh to 1°W.I. we can see some difference between the reference line, and the one marked in present work. In particular, the literature reference indicates the approximate limit of $\mathrm{We}_{g,\mathrm{lim}} \simeq 1.2$, obtained from linear stability considerations by Sterling and Sleicher [43]. According to our study, transition occurs at $\mathrm{We}_{g,\mathrm{lim}} \simeq 2.1$, as clearly visible in Fig. 20.

In the analysis of the more unstable regimes, we observed that Tests 4 and 5, characterized by the unstable growth of instabilities and the irregular rupture of the liquid core, lie both inside 1°W.I.. Test 5–b and Test 6 correctly belong to 2°W.I., as they present, in addition to irregular surface fluctuations, a sustained peeling-off of droplets from the jet surface and tip. Finally, Tests 6–b, 7 and 8 are clearly within the atomization regime, as demonstrated by the decay of the jet structure into a fine dispersion of particles. Hence, the two limits representing the transitions between 1°W.I. and 2°W.I. (formulated by Ranz [42]), and from 2°W.I. to Atomization (com-

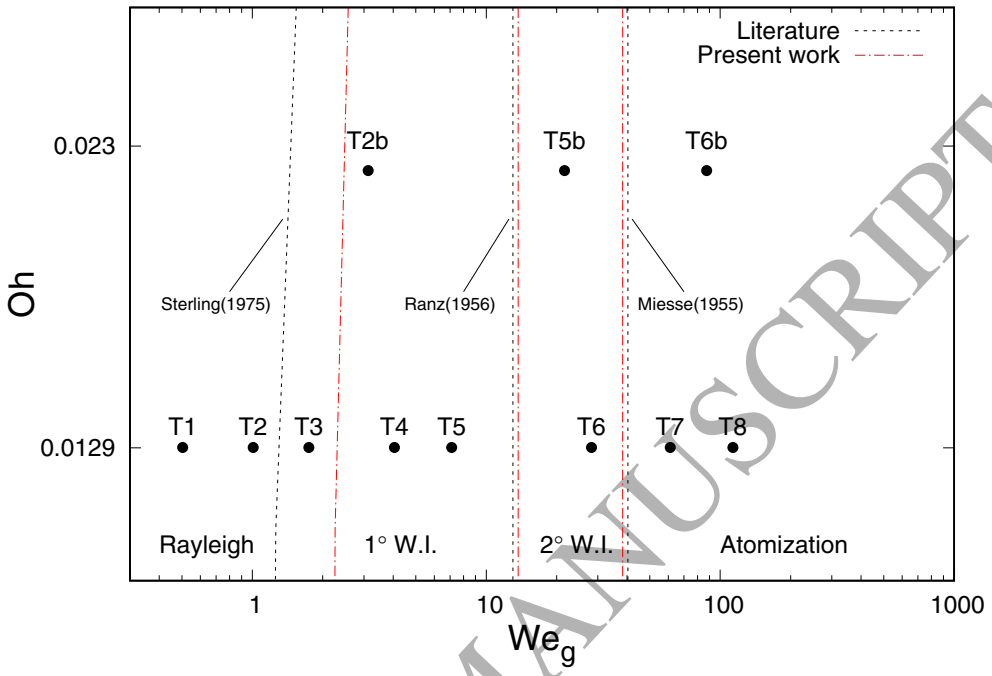

Figure 20: Atomization regime map as a function of We_g and Oh. Black points represent the cases analyzed by means of numerical simulations in the present work. Black lines are the regime transition lines obtained from literature and exposed in Sec. 4. Red lines represent the approximate transition zones observed in our simulations.

ing from empirical considerations by Miesse [44]), are well approximated by numerical simulations. This is clearly highlighted in both Figs. 20 and 21 by the proximity of black and red lines.

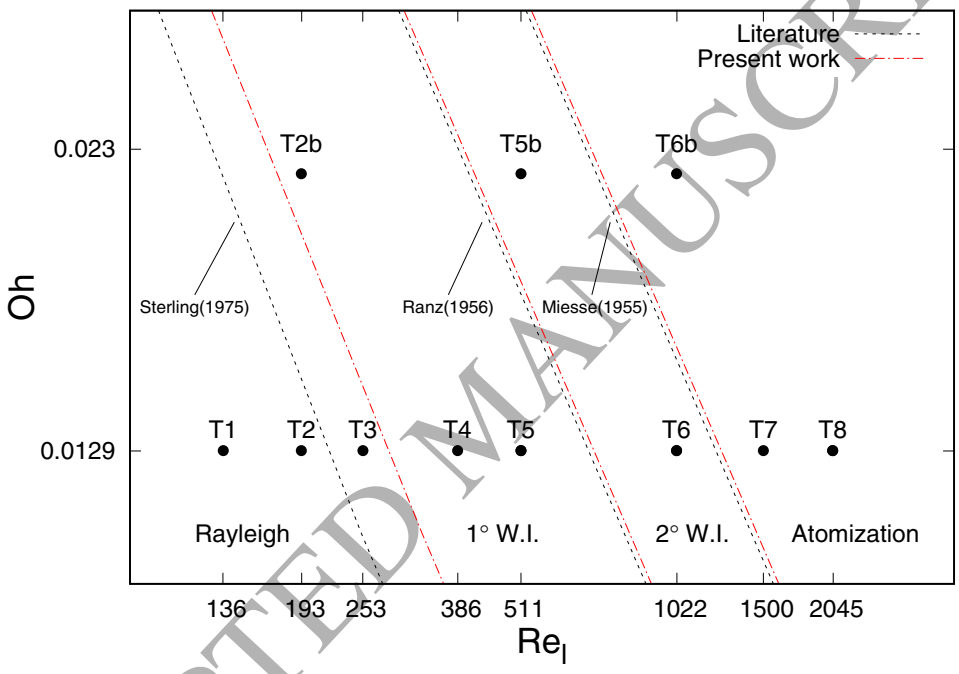

Figure 21: Atomization regime map as a function of Re_l and Oh. Black points represent the cases analyzed by means of numerical simulations in the present work. Black lines are the regime transition lines obtained from literature and exposed in Sec. 4. Red lines represent the approximate transition zones observed in our simulations.

6. Conclusions

In this paper we adopt a finite-volume numerical strategy to perform the DNS of different 3D Liquid Injection phenomena. The strategy accounts for the non-filtered resolution of momentum conservation equations and for a Conservative Level-Set interface-capturing scheme, implemented by Balcázar et al. [19] on collocated unstructured meshes. We integrate the solver with the Adaptive Mesh Refinement (AMR) algorithm developed by Antepara et al. [20], in order to optimize the employed computational resources. The proposed framework has already demonstrated its reliability in general multiphase and unstable phenomena in past works [21, 22]. Moreover, in Schillaci et al. [23] we used the same strategy to carry out the complete simulation of a 2D Coaxial Jet in a turbulent scenario.

In Sec. 3, the described model is applied and verified in the context of 3D atomizing flows by simulating the 3D Coaxial Liquid-Air Jets at Re_l=600 and $\mathrm{Re}_l \simeq 1.0 \times 10^4$, respectively. The simulations are validated by measuring some physical features of the flow, and comparing them with experimental sources. In particular, in the near-field test, where the primary instabilities lead to the core break-up, we have measured the wavelengths connected to both Kelvin-Helmholtz and Rayleigh-Taylor instabilities, finding good agreement with the semi-empirical correlations proposed by Marmottant and Villermaux [27]. Hence, in a second test, we focused on the study of the far-field region, where the secondary structures have mostly degraded into droplets. Here we have evaluated the statistical distribution of droplets,

obtaining a Sauter Mean Diameter close to that indicated by [27].

The main part of the work consists in the assessment of the physics of Liquid Injection into a stagnant air environment. After introducing the theoretical and experimental studies concerning the physics of liquid sprays in Sec. 4, we conducted a series of simulations to analyze their physical behavior as function of different input parameters. In a first study (Tests 1–8), Sec. 5.2, we analyzed the variation of the break-up regime according to the input speed, with Reynolds number ranging between $\mathrm{Re}_l = 136 : 2045$. The characteristics of the various regimes encountered when increasing Re_l are consistent with the observations made in various studies [40, 37, 38], allowing to qualitatively recognize the four stages of instability of a jet: Rayleigh, 1°and 2° Wind-Induced and Atomization. In the same Section, we give computational details and statistics of the performed simulations, and we report the study of the mean droplet size as function of x/D for the cases belonging to the Atomization regime. We assessed the capability of our method of reproducing the competition mechanism between break-up and coalescence of droplets in the far-field of the jet, phenomenon previously indicated by Lasheras and Hopfinger [26].

In Sec. 5.3 the variation of the intact-length of the jet, L/D, as function of the inlet jet velocity is studied, showing a partial agreement with the experiments made by Badens et al. [17]. In particular, in Rayleigh and 1° W.I. regimes, L/D measured in simulations is close to that of [17], demonstrating that for low Re_l conditions, the inlet condition of the jet does not affect the

break-up mechanism. On the other hand, a certain discrepancy is noticed for intermediate Re_l, as the intact-length observed in simulations results longer then the experimental ones. This is probably due to a certain discrepancy in the inlet velocity profile between numerical and experimental set-up. Indeed, the imposed numerical inlet profile is regular, while velocity fluctuations caused by the mechanical injection system in the experimental set-up may favour a shortening of the break-up length.

Further simulations were performed by varying the magnitude of the surface tension coefficient in some selected cases, leading to the additional observations reported in Sec. 5.4.

Finally, in Sec. 5.5, the simulations reported in Secs. 5.2 and 5.4 have been collected and placed inside the We_g vs. Oh and the Re_l vs. Oh Regime Maps. In the transitions between 1°and 2° W.I., and between 2° W.I. and Atomization zones we observed good agreement between the numerical simulations and the correlations found in the literature. A small discrepancy was found in the limit Weber number marking the transition between Rayleigh and 1° Wind-Induced regime ($\mathrm{We}_{g,\mathrm{lim}} \simeq 1.2$ [43] vs. $\mathrm{We}_{g,\mathrm{lim}} \simeq 2.1$ [present work]).

Acknoledgements

This work has been financially supported by the Ministerio de Economía y Competitividad, Secretaría de Estado de Investigacíon, Desarrollo e Innovacíon, Spain (ENE2015-70672-P,ENE17-88697-R) and by Termo Fluids

S.L. The author Eugenio Schillaci acknowledges financial support in form of a doctoral scholarship (FI Grant, 2014-FI-B01232) provided by AGAUR (Generalitat de Catalunya). Computer resources at MareNostrum III and IV, with technical support provided by BSC (RES-FI-2016-1-0023, RES-FI-2017-2-0015) and at FinisTerrae II, with support by CESGA (RES-FI-2016-2-0028, RES-FI-2016-3-0015) are acknowledged.

References

[1] G. Tryggvason, R. Scardovelli, S. Zaleski, Direct numerical simulations of gas–liquid multiphase flows, Cambridge University Press, 2011.

[2] A. Vallet, A. Burluka, R. Borghi, Development of a eulerian model for the atomization of a liquid jet, Atomization and Sprays 11 (2001) 619–642.

[3] M. Gorokhovski, M. Herrmann, Modeling primary atomization, Annual Review of Fluid Mechanics 40 (2008) 343–366.

[4] P. Sagaut, Large eddy simulation for incompressible flows: an introduction, Springer Science & Business Media, 2006.

[5] P. Liovic, D. Lakehal, Multi-physics treatment in the vicinity of arbitrarily deformable gas–liquid interfaces, Journal of Computational Physics 222 (2007) 504–535.

[6] M. Behzad, N. Ashgriz, B. Karney, Surface breakup of a non-turbulent liquid jet injected into a high pressure gaseous crossflow, International Journal of Multiphase Flow 80 (2016) 100–117.

[7] J. Shinjo, A. Umemura, Simulation of liquid jet primary breakup: Dynamics of ligament and droplet formation, International Journal of Multiphase Flow 36 (2010) 513–532.

[8] O. Desjardins, V. Moureau, H. Pitsch, An accurate conservative level set/ghost fluid method for simulating turbulent atomization, Journal of Computational Physics 227 (2008) 8395–8416.

[9] O. Desjardins, J. McCaslin, M. Owkes, P. Brady, Direct numerical and large-eddy simulation of primary atomization in complex geometries, Atomization and Sprays 23 (2013).

[10] T. Ménard, S. Tanguy, A. Berlemont, Coupling level set/vof/ghost fluid methods: Validation and application to 3d simulation of the primary break-up of a liquid jet, International Journal of Multiphase Flow 33 (2007) 510–524.

[11] R. Lebas, T. Menard, P.-A. Beau, A. Berlemont, F.-X. Demoulin, Numerical simulation of primary break-up and atomization: Dns and modelling study, International Journal of Multiphase Flow 35 (2009) 247–260.

[12] D. Fuster, A. Bagué, T. Boeck, L. Le Moyne, A. Leboissetier, S. Popinet, P. Ray, R. Scardovelli, S. Zaleski, Simulation of primary atomization with an octree adaptive mesh refinement and vof method, International Journal of Multiphase Flow 35 (2009) 550–565.

[13] J. Delteil, S. Vincent, A. Erriguible, P. Subra-Paternault, Numerical investigations in rayleigh breakup of round liquid jets with vof methods, Computers & Fluids 50 (2011) 10–23.

[14] F. Salvador, J. Romero, M. Roselló, D. Jaramillo, Numerical simulation of primary atomization in diesel spray at low injection pressure, Journal of Computational and Applied Mathematics 291 (2016) 94–102.

[15] H. Grosshans, A. Movaghar, L. Cao, M. Oevermann, R.-Z. Szász, L. Fuchs, Sensitivity of VOF simulations of the liquid jet breakup to physical and numerical parameters, Computers & Fluids 136 (2016) 312–323.

[16] C. Shao, K. Luo, Y. Yang, J. Fan, Detailed numerical simulation of swirling primary atomization using a mass conservative level set method, International Journal of Multiphase Flow 89 (2017) 57–68.

[17] E. Badens, O. Boutin, G. Charbit, Laminar jet dispersion and jet atomization in pressurized carbon dioxide, The Journal of supercritical fluids 36 (2005) 81–90.

[18] Termo fluids s.l., webpage: www.termofluids.com, ????

[19] N. Balcázar, L. Jofre, O. Lehmkuhl, J. Castro, J. Rigola, A finite-volume/level-set method for simulating two-phase flows on unstructured grids, International Journal of Multiphase Flow 64 (2014) 55–72.

[20] O. Antepara, O. Lehmkuhl, R. Borrell, J. Chiva, A. Oliva, Parallel adaptive mesh refinement for large-eddy simulations of turbulent flows, Computers & Fluids 110 (2014) 48–61.

[21] E. Schillaci, O. Antepara, O. Lehmkuhl, N. Balcázar, A. Oliva, Effectiveness of adaptive mesh refinement strategies in the DNS of multiphase flows, in: Proceedings of International Symposium Turbulent Heat and Mass Transfer VIII, 2015.

[22] E. Schillaci, O. Lehmkuhl, O. Antepara, A. Oliva, Direct numerical simulation of multiphase flows with unstable interfaces, Journal of Physics: Conference Series 745 (2016).

[23] E. Schillaci, L. Jofre, N. Balcázar, O. Antepara, A. Oliva, A low-dissipation convection scheme for the stable discretization of turbulent interfacial flow, Computers & Fluids 153 (2017) 102–117.

[24] N. Balcázar, J. Rigola, J. Castro, A. Oliva, A level-set model for thermocapillary motion of deformable fluid particles, International Journal of Heat and Fluid Flow 62 (2016) 324–343.

[25] E. Gutiérrez, N. Balcázar, E. Bartrons, J. Rigola, Numerical study of

taylor bubbles rising in a stagnant liquid using a level-set/moving-mesh method, Chemical Engineering Science 164 (2017) 158 – 177.

[26] J. Lasheras, E. Hopfinger, Liquid jet instability and atomization in a coaxial gas stream, Annu. Rev. Fluid Mech. 32 (2000) 275–308.

[27] P. Marmottant, E. Villermaux, On spray formation, J. Fluid Mech. 498 (2004) 73–111.

[28] E. Olsson, G. Kreiss, A conservative level set method for two phase flow, Journal of Computational Physics 210 (2005) 225–246.

[29] M. Sussman, E. G. Puckett, A coupled level set and volume-of-fluid method for computing 3d and axisymmetric incompressible two-phase flows, Journal of computational physics 162 (2000) 301–337.

[30] N. Balcázar, O. Lehmkuhl, L. Jofre, J. Rigola, A. Oliva, A coupled volume-of-fluid/level-set method for simulation of two-phase flows on unstructured meshes, Computers & Fluids 124 (2016) 12 –29.

[31] Z. Wang, J. Yang, B. Koo, F. Stern, A coupled level set and volume-of-fluid method for sharp interface simulation of plunging breaking waves, International Journal of Multiphase Flow 35 (2009) 227–246.

[32] J. Brackbill, D. B. Kothe, C. Zemach, A continuum method for modeling surface tension, Journal of Computational Physics 100 (1992) 335–354.

[33] C. Varga, J. C. Lasheras, E. Hopfinger, Initial breakup of a small-diameter liquid jet by a high-speed gas stream, Journal of Fluid Mechanics 497 (2003) 405–434.

[34] F. B. Rayana, A. Cartellier, E. Hopfinger, et al., Assisted atomization of a liquid layer: investigation of the parameters affecting the mean drop size prediction, in: Proceedings of the International Conference on Liquid Atomization and Spray Systems (ICLASS), Kyoto, Japan, 2006.

[35] Webpage: www.cttc.upc.edu, ????

[36] Webpage: www.cesga.es, ????

[37] G. Faeth, Structure and atomization properties of dense turbulent sprays, in: Symposium (International) on Combustion, volume 23, Elsevier, 1991, pp. 1345–1352.

[38] C. Dumouchel, On the experimental investigation on primary atomization of liquid streams, Experiments in fluids 45 (2008) 371–422.

[39] J. Eggers, E. Villermaux, Physics of liquid jets, Reports on progress in physics 71 (2008) 036601.

[40] R. Reitz, F. Bracco, Mechanism of atomization of a liquid jet, The Physics of Fluids 25 (1982) 1730–1742.

[41] M. McCarthy, N. Molloy, Review of stability of liquid jets and the

influence of nozzle design, The Chemical Engineering Journal 7 (1974) 1–20.

[42] W. Ranz, On sprays and spraying, Dep. Eng. Res., Penn State Univ. Bull 65, 1956.

[43] A. M. Sterling, C. Sleicher, The instability of capillary jets, Journal of Fluid Mechanics 68 (1975) 477–495.

[44] C. Miesse, Correlation of experimental data on the disintegration of liquid jets, Industrial & Engineering Chemistry 47 (1955) 1690–1701.

[45] Webpage: www.bsc.es, ????

[46] J. Lasheras, E. Villermaux, E. Hopfinger, Break-up and atomization of a round water jet by a high-speed annular air jet, Journal of Fluid Mechanics 357 (1998) 351–379.